Synthesis of titanium dioxide nanoparticles using a curved-wall jet burner with central port

Mohamed A. Ismail[*, 1], Morkous S. Mansour[1,2], Nasir K. Memon[3], Suk Ho Chung[1]

[1]Clean Combustion Research Center, King Abdullah University of Science and Technology, Thuwal, Saudi Arabia
[2]Department of Mechanical Engineering, Helwan University, Cairo, Egypt
[3]Qatar Environment and Energy Research Institute, Qatar Foundation, Doha, Qatar

Abstract

A curved-wall jet (CWJ) burner was modified and designed for flame synthesis. A central port with puppet valve type of opening was used to deliver the precursor tangentially to the cavity region of the recirculating flow in the recirculation zone. This modified CWJ burner demonstrated appreciable mixing characteristics between the precursor and combustion gases within these regions, with a slight decrease in the axial velocity due to the precursor injection. The burner produced highly crystallined TiO_2 nanoparticles with size distribution range of 18-26 nm and the phase was mainly dependent on the equivalence ratio. Reynolds number was found to slightly affect the phase content of the TiO_2.

Introduction

Titanium oxide (TiO_2) particles have drawn worldwide interest in oxide semiconductors for future applications related to photocatalytic water splitting [1, 2], die-synthesized solar cells [3], and other photocatalytic applications [4]. Rutile phase of TiO_2 is mainly used for pigments while the anatase phase plays an important role in the photocatalytic applications.

In laboratory scale studies, small laminar flames have been typically used to investigate the growth process of TiO_2 nanoparticles [5-7], whereas industrial processes of flame synthesis use large scale turbulent burners [8]. Such growth process is strongly influenced by flow and flame conditions and appreciably differs when comparing laminar with turbulent flames. Systematic lab-scale experiments involving turbulent flames are required to enhance our understanding of nanoparticle formation, which will help to control crystallinity, size, and morphology of nanoparticles produced in flames.

Many parameters are controlling the growth of nanoparticles such as burner geometry, fuel/oxidizer flow rates, precursor loading rate, residence time, and fuel type [6]. Common fuels investigated include carbon monoxide [9], hydrogen [10], methane [3], propane [11] and ethylene [12]. Of particular interest is the use of propane, as it can further reduce the cost of flame synthesized nanoparticles. Moreover, nanoparticles produced using a propane/air mixture resulted in nanoparticles with properties comparable to commercially made Degusa P25 TiO_2 [13].

For the scale-up of flame synthesis in a laboratory, we have previously adopted a curved-wall jet (CWJ) burner for nanoparticle synthesis by injecting precursors through a center tube and by supplying fuel/air mixtures as an annular-inward jet for rapid mixing of the precursors in the reaction zone [12]. Nanoparticles were produced in ethylene (C_2H_4)/air premixed flames using titanium tetraisopropoxide (TTIP) and hexamethyldisiloxane (HMDSO) as the precursors for TiO_2 and SiO_2 nanoparticles, respectively. Particle image velocimetry measurements confirmed that the precursors can be injected into the flames without appreciably affecting flow structure. Temperature, residence time and equivalence ratio were found to be the major control parameters for the growth of the nanoparticles and their phase. Particles produced using the CWJ burner exhibited a bimodal size distribution due to non-uniform residence time in the high temperature zone along the radial plane above the burner [14]. This is because the flow through the central port obstructs the formation of recirculating flow inside the cavity.

In this study, we modified the burner to have a flow guide having a puppet valve type on top of the central port for the precursor delivery such that the precursor flow is aiding the recirculating flow in the cavity region. Thus, the main flow of premixture of fuel and air from the curved-wall slit and the precursor flow from the central port are aiding each other in forming a recirculation zone to support the flame. Consequently, the precursor can be well-mixed with the recirculating burnt gases and is distributed reasonably uniformly in the main flame region. The influences of various operating parameters (equivalence ratio and Reynolds numbers) as well as the precursor's Reynold number were investigated using ethylene and propane fuels. Only the ethylene fuel cases are reported in this paper.

Experiment

The apparatus consisted of a curved-wall jet burner, a precursor delivery system, a nanoparticle collection system, and high-speed PIV and OH PLIF setups. The burner, as schematically shown in Fig. 1, is composed of a center body of a cylinder (ϕ50 mm) with a hemi-spherical tip, and an outer cylinder with curved-

[*] Corresponding Author: Mohamed.ismail@kaust.edu.sa

converging section having an exit diameter of ϕ43 mm. The slit width between the center body and the outer cylinder is 0.8 mm and is long enough to prevent any flashback. This slit is used for the reactants (fuel/air) supply. A concave spherical cavity with R56 mm was created on top of the hemi-sphere (3.37 mm in depth and 24 mm in width at the tip) for better flame stabilization [15, 16] by promoting a recirculation zone. The height of the outer cylinder is adjustable. The converging section between the two cylinders guided fuel and air tangentially to the curved wall of the center body toward the axis to form an annular-inward jet. A central port of 10 mm in diameter was machined in the center body. A puppet valve type flow guide was placed on top of the central port having 2 mm gap for the precursor delivery to direct the precursor tangentially into the recirculation zone for better mixing. The burner surface was anodized to minimize light reflection.

Ethylene (99.995%) and air premixtures were supplied through the curved wall slit of the burner. Titanium tetraisopropoxide (TTIP) was used as the nanoparticle precursor, which was heated in a bubbler to 110^{o}C and the vapor was carried with nitrogen at a fixed loading of 2 SLPM and supplied through the central port of the burner. The precursor delivery line after the bubbler was heated to 180 ^{o}C to prevent condensation. Experiments were conducted by varying flow rates as well as equivalence ratio. Flames with various equivalence ratios are denoted as F1 to F4, whereas F5 to F7 refer to flames with various Reynolds numbers (see Table 1 for operating conditions). All the flames listed in Table 1 have the Re for the precursor $Re|_{Pre}$= 108 based on the carrier gas flow rate and the exit area between the puppet valve and the central port. The generated nanoparticles were collected on glass-fiber filters using a vacuum pump. All experiments were conducted at atmospheric pressure.

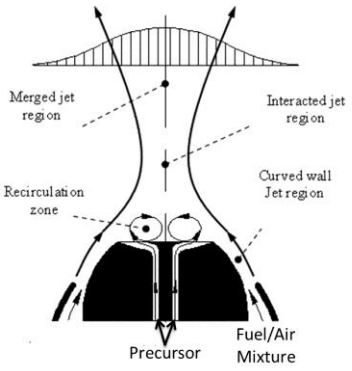

Figure 1: Schematic diagram of curved-wall jet burner with central port exhibiting the flow field.

Visible flame height was measured using a cathetometer and the results were compared with the average values obtained from photographs. The PIV system consisted of a high-repetition rate twin-cavity diode-pumped Nd:YLF laser (Litron, LDY304-PIV; 527 nm, 28 mJ/pulse, 5 ns pulse duration) and a CMOS camera (LaVision, Imager Pro HS 4M; 2016×2016 pixels) coupled with a controller. Double-pulses with a time separation of 20-40 μs were repeated at 1 kHz. The laser output formed a sheet approximately 1 mm in thickness and 100 mm in height by a series of lenses. Seed particles were titanium dioxide (TiO_2, nominal diameter 0.18 μm) and the seed levels were adjusted for spurious vectors in the image processing to be less than 5%. A perspective distortion from the camera system was calibrated by imaging a 3-D dot target (LaVision type 11). Velocity fields were determined through multi-pass vector computation software (Davis 8.1) with an interrogation size of 32×32 pixels and 50% overlap, yielding a 0.76×0.76 mm^2 spatial resolution.

The high-speed planar laser-induced fluorescence system consisted of a diode-pumped Nd:YAG laser (Edgewave, IS16II-E; 532 nm) and a dye laser (Sirah, Credo-Dye) whose output was frequency-doubled to 283.57 nm to excite $Q_1(8)$ line of A-X (1,0) OH transition with about 0.3 mJ/pulse at 10 kHz repetition rate. OH signals were detected at 295-345 nm with an intensified CMOS camera (Lavision, HSS8 and IRO; 1024×1024 pixels). Elastic scattering noise from the laser sheet and background noise were reduced by using a band-pass filter (>80% at 320 nm) and also by minimizing the intensifier gate time (200 ns). The spatial resolution was 0.11 mm/pixel.

Table 1: Operating conditions and summary of results for various flames.

Flame	Re	ϕ	H [mm]	τ [ms]	Anatase %
F1	13,142	1.2	138.1	8.85	69.9
F2		1.3	157.8	9.85	74.4
F3		1.6	214.8	12.40	86.2
F4		1.8	235.1	12.99	94.2
F5	8,300	1.3	148.3	13.25	80.2
F6	9,130		154.6	11.2	81.5
F7	18,676		160.3	7.17	72.3

The collected nanoparticles were characterized using X-ray diffraction (XRD) by an advance X-ray powder diffractometer (Bruker, D8) with CuKα (λ=1.5406 Å) radiation. Raman spectroscopy measurements were performed on a Raman spectrometer (Aramis, LabRAM HR Visible) using 473 nm excitation from a diode-pumped solid-state (DPSS) laser (7 mW with 1.1 cm^{-1} spectral resolution). The primary particle size and morphology were examined by transmission electron microscopy (TEM) and high-resolution TEM (HRTEM) (FEI Titan, G2 80-300). The particle size distribution was measured using Zeta Sizer (Malvern Instruments Ltd.) using ethanol as the dispersant for the nanoparticles.

Results and Discussion

Flame and flow characteristics

Basic flame features are discussed first to characterize the burner, including flame shape and reactive flow field characteristics.

Photographs of flames stabilized in the burner are shown in Fig. 2 at several operating conditions listed in Table 1 without (upper row) and with (lower row) precursor supply for the mixture Reynolds number (Re) based on jet velocity, mixture kinematic viscosity, and hydraulic diameter at jet exit of 60 mm was 13,142. The equivalence ratio ϕ was varied from 1.2 to 1.8 using ethylene fuel.

The precursor Reynolds number was also changed from 108 to 178.

These flames have blue color with crown shape which stabilizes the flame by the formation of a recirculation zone. Previous studies [12, 15, 16] showed that the flame height measured from the tip of the concave cavity increases with equivalence ratio. The present flames are in accordance with this behavior. Although not shown, the effect of Reynolds number was also tested ranging from 8,300 to 18,676, which has a small effect on the flame height (H changed by < 6% with respect to Re).

When TTIP is added to these flames, they become more luminous, attributed to nanoparticles formation and surface radiation in these flames. The flame heights, H, (for flames without precursor addition) are in the range of about 138-236 mm (Table 1), an increase in flame height being exhibited with increase in equivalence ratio; this is reasonable since more air is required to burn the fuel. Also, a slight increase in the flame height is realized due to the increase of Re because of the increased heat flux entering the reaction region in the flame.

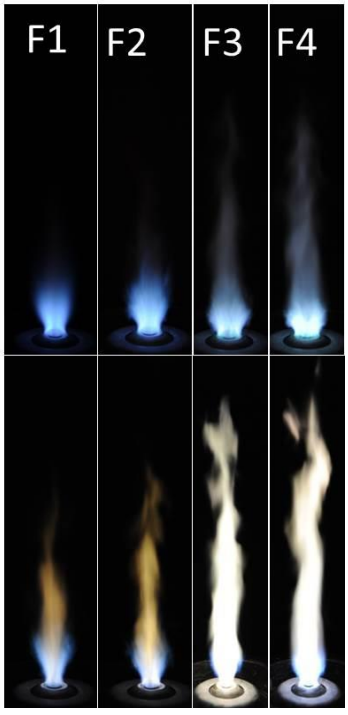

Figure 2: Direct flame images showing the effect of equivalence ratio at Re= 13,142 flames, top row without precursor and bottom row with precursor.

The PIV system was used to characterize the turbulent flow field. Figure 3 shows the time-averaged mean velocity vector fields for the rich (ϕ=1.8) ethylene flame and Re = 19,871 with (a) and without (b) TTIP precursor, with the background color indicating velocity magnitude. Also shown are the typical streamlines in white color. The general features of the flow field exhibit typical flow characteristics of the CWJ burner [15, 16]. The flow field consists of a recirculation zone (RZ), an interaction jet (IJ) region with the collision of the annular-inward jets near y = 6 mm, and a downstream merged jet (MJ) region. The velocity of the annular slit jet decreases toward the wall and ambient side, thus inner and outer shear layers (ISL and OSL) are surrounding the annular-inward jets (AJ) . The velocity gradients in these shear layers could generate turbulence, augmented by the collision of annular-inward jets. TTIP precursor has decreased the magnitude of the maximum velocity vector when it is supplied to the burner through the inner slit by small percentage (< 8%). This can be attributed to its entrainment in the recirculation zone opposing the main flow and reducing its velocity. Because the precursor's Re is very low compared to the flow Re, this effect is small.

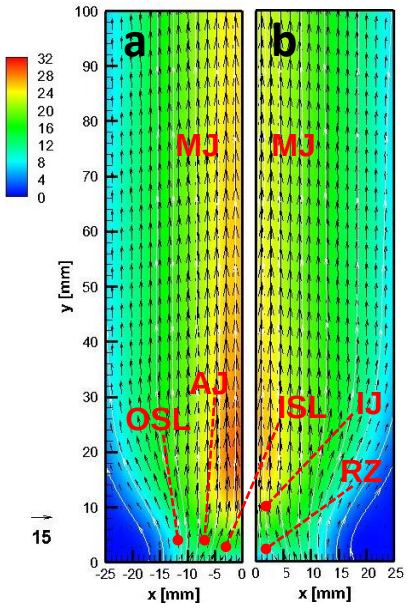

Figure 3: Time averaged velocity vector plot of flow field for a flame with ϕ=1.8 and Re= 19,871; (a) without and (b) with TTIP precursor (white lines indicate streamlines).

The axial profiles of the mean flow velocities, v, (at the burner's centerline) are plotted in Fig. 4. In the interaction jet region, v increases rapidly and then slightly decreases (F2 and F7) or maintains near uniform values (F5 and F6) up to y = 100 mm in the merged jet region. TTIP precursor has only small influence on the velocity values for F5 and F7 flames.

Such velocity quantification and visible flame height enabled in estimating the total residence time of the

precursor within the hot gases. These are 8.85 and 13.25 ms corresponding to flames F1 and F5, respectively, as reported in Table 1. The increase in residence time with increasing ϕ using ethylene fuel is expected to increase the anatase content as concluded in our previous work [12].

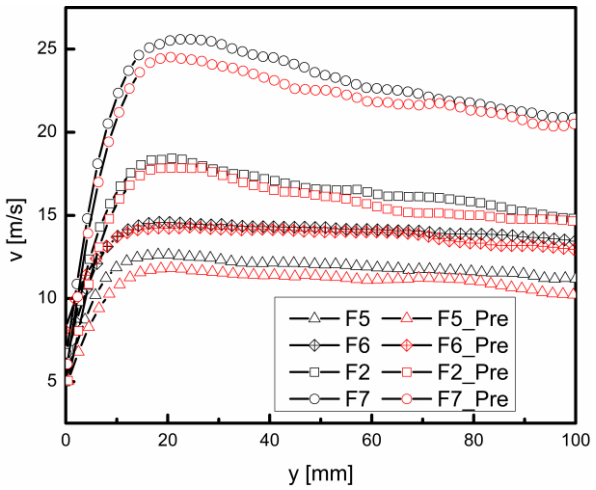

Figure 4: Axial profiles of flow velocity along the burner centerline (Pre denotes with TTIP precursor).

The time resolved, 10 kHz, OH-PLIF system was employed to provide insights on various dynamics of turbulent premixed flames and to investigate the flames structure. Figure 5 shows typical images of OH-PLIF (F5 and F7). The instantaneous images of OH reveal the existence of a recirculation zone upstream at the concave cavity followed by, for high Re flames (F7), thin necking zone at the interaction jet region and then the highest OH signal zone further downstream. TTIP precursor has a slight effect on the flame structure particularly F5 as there is a region without OH signal.

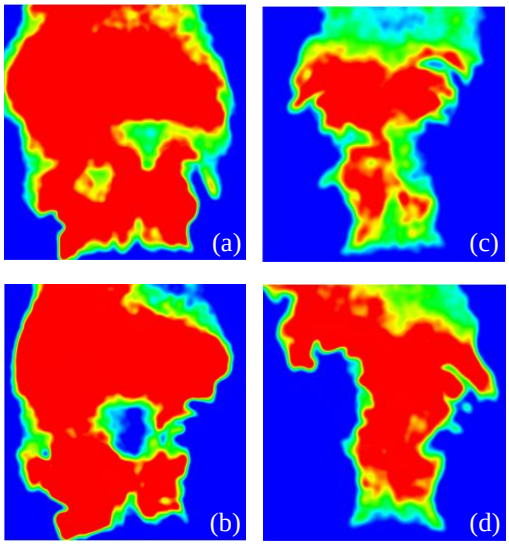

Figure 5: OH-PLIF images for flames F5 (a,b) and F7 (c,d) without (upper) and with (lower) TTIP precursor, showing their flame structure.

These images provide the following features: (1) the recirculation zone is somewhat clear and confined within the burner tip for flame F5; however, it moves slightly downstream in F7; (2) the production of OH radical in the recirculation zone is appreciably influenced in flames with precursor (Fig. 5b and d); (3) the wrinkled reaction sheets distribute predominantly along the shear layers in high Re flames (F7), however, in low Re flames (F5), less-wrinkled reactions zones appear further downstream associated with the abundance of OH species; (4) These images imply that flames are attached to the burner tip as they have high flame speed.

Nanoparticle characterization

TTIP (with loading rate of 50 g/hr based on vapor pressure [17]) and nitrogen carrier gas flow rate of 2 SLPM were used to synthesize titanium dioxide (TiO_2) nanoparticles. TiO_2 nanoparticles were collected and analyzed with the XRD at several operating conditions from which the crystal phase, average crystallite size, and rutile/anatase phase ratio could be determined.

Fig. 6 shows the XRD pattern for different equivalence ratios at Re=13,142. For all cases, both the peaks representing the anatase (A) and rutile (R) phases can be seen, an indication of the mixture of these two phases. The anatase to rutile ratio in the samples was calculated by integrating the respective XRD peak intensities (anatase and rutile peaks at 2θ = 25.4 and 27.5°, respectively). It is clear from the relative anatase and rutile peak intensities that the percentage of anatase in the mixture increases with increasing ϕ in accordance with the increase in the residence time [12]. The values of anatase percentage in the mixture are listed in Table 1 and represented in Fig. 7, which shows near linear dependence on equivalence ratio.

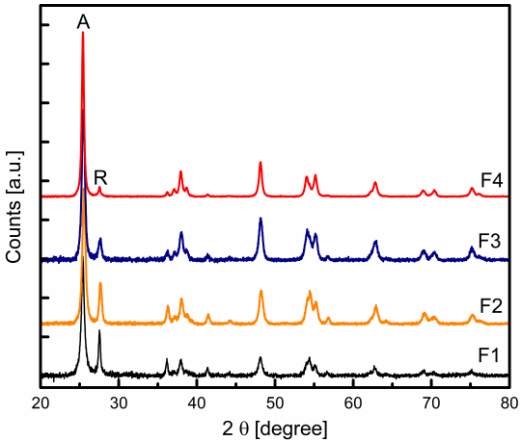

Figure 6: XRD pattern for TiO_2 NP synthesized using ethylene flames at different equivalence ratios (A and R stand for the first anatase and rutile peaks, respectively).

The Reynolds number has a small effect on the anatase content (Fig. 7). As Re increases from 8,300 to 18,676 the anatase content decreases by about 8%

because of shorter residence time in the high temperature region. The effect of the precursor's Reynolds number $Re|_{Pre}$ was also investigated by changing the area between the puppet valve and the central port (area for precursor delivery). $Re|_{Pre}$ was changed from 108 to 187 at ϕ=1.8 and Re=13,142. The influence on anatase content was negligible, changing from 94.2 to 93.5 for $Re|_{Pre}$ of 108 1nd 187, respectively.

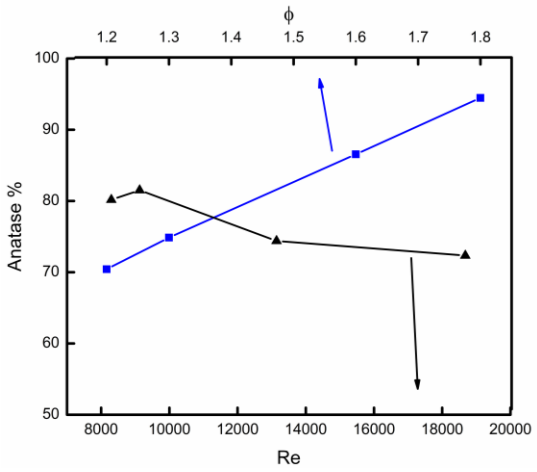

Figure 7: Effect of equivalence ratio and Re on the anatase content for different ethylene flames.

To further examine the phases of TiO_2 nanoparticles, the Raman spectroscopy measurements were performed. The visible region of the Raman spectra at different flames was determined. Although not shown here, the peaks for flames F1 and F2 correspond to the Raman modes of both anatase and rutile phases, whereas for F4 flame all peaks correspond to the anatase phase. This result is consistent with XRD data shown previously, where the predominant phase at higher equivalence ratio is the anatase phase.

The primary particle size was calculated from the XRD results using Scherrer's eq. [18] and found to be in the range of 18- 26 nm. The particle size was slightly affected by ϕ or Re in the tested range. The aggregate size was measured using Zeta Sizer and found to have a single peak of particle size distribution (NOT shown here) around 95 nm. This result indicates that the aggregation ratio of the produced TiO_2 nanoparticles is about 3.6 which is acceptable for those generated by flames. This small range of size distribution with a single peak is a favorable advantage of the present configuration (puppet valve on top of the central port) as compared with the previous work [12].

The high resolution TEM images of TiO_2 nanoparticles for flames F1 and F3 are shown in Fig. 8. The particles are mostly spherical with some polyhedral shapes. The images reveal the high crystallinity and the ordered structure of the nanoparticle lattice planes in addition to some amorphous particles. By increasing the equivalence ratio to values higher than 1.6, a planar defect in some of the generated nanoparticles starts to appear in the HRTEM image (Fig. 8.b). The average particle diameter calculated from TEM images has the value of 30 nm with some smaller particles which agrees with the results obtained from XRD experiments.

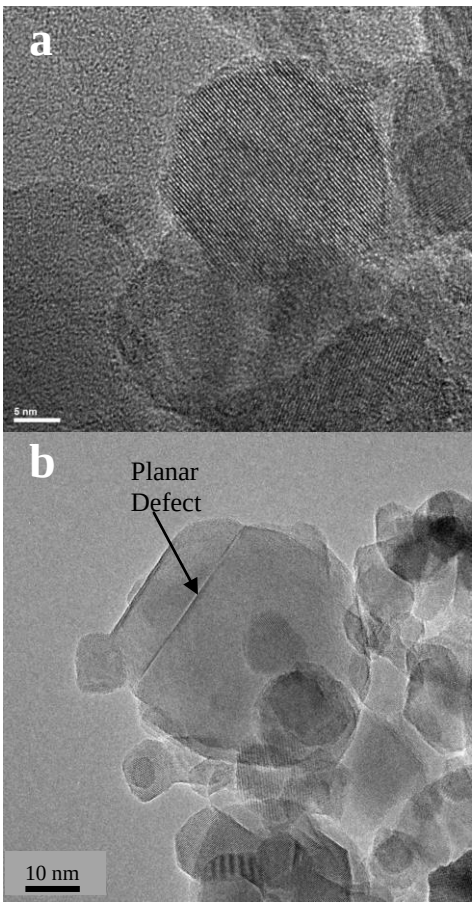

Figure 8: High resolution TEM for TiO2 particles synthesized using flame (a) F1 and (b) F3 ethylene flames.

The planar defects located close to the boundary of the nanoparticle (not in the middle), which suggests that the planar defects were produced just before the complete growth of the nanoparticle [19]. The ratio of particles with a planar defect is very small compared to the total number of particles. The planar defects might be formed due to oriented attachment and growth including twin planes and other interfaces [20]. These microstructures are consequence of coarsening mechanism that involves the reduction of surface tension through elimination of surfaces by attachment. The structurally different region (defect) may serve as a nucleation site for new phases.

Conclusions

The usefulness of the curved-wall jet (CWJ) burner with a puppet valve shaped guide on top of the central port has been demonstrated for material synthesis of nanoparticles. The growth of TiO_2 nanoparticles has been reported with some key points affecting this growth. First, The CWJ burner can operate at a wide

range of equivalence ratios and was found to exhibit small size turbulent flame characteristics. PIV data confirmed this behavior and the precursor flow had little impact on the flame behavior. Second, the crystal phase of the TiO_2 nanoparticles was strongly dependent on the equivalence ratio. At higher values, due to a longer residence time in high temperature region, the growth of anatase nanoparticles was dominant (flame F4). Finally, this configuration of the CWJ burner has a narrow range of particle size distribution (18-25 nm) with aggregation ratio of 3.6, which showed better results as compared with the original CWJ burner.

Acknowledgement

This work was supported by Competitive Research Funding from King Abdullah University of Science and Technology. We are grateful to Dr. Dalaver Anjum at the Nanofabrication and Imaging Lab at King Abdullah University of Science and Technology for his great efforts and help to get the high resolution TEM images.

References

1. A. L. Linsebigler; G. Lu; J. T. Yates Jr, Chem. Rev. 95 (3) (1995) 735-758.
2. PJD Lindan, NM Harrison, JM Holender, MJ Gillan, Chem. Phys. Lett. 261 (3) (1996) 246-252.
3. M. Grätzel, Nature 414 (6861) (2001) 338-344.
4. X. Nie, S. Zhuo, G. Maeng, K. Sohlberg, Int. J. Photoenergy 2009 (2009).
5. S. E. Pratsinis; W. H. Zhu; S. Vemury, Powder Technol 86 (1) (1996) 87-93.
6. N. K. Memon; D. H. Anjum; S. H. Chung, Combust. Flame 160 (9) (2013) 1848-1856.
7. D. H. Anjum; N. K. Memon; S. H. Chung, Mater. Lett. 108 (2013) 134-138.
8. H. K. Kammler; L. Madler; S. E. Pratsinis, Chem Eng Technol 24 (6) (2001) 583-596.
9. A. George; R. Murley; E. Place, Faraday Symposia of the Chemical Society, 1973; Royal Society of Chemistry (1973) 63-71.
10. M. Formenti; F. Juillet; P. Meriaudeau; S. J. Teichner; P. Vergnon, J. Colloid Interface Sci. 39 (1) (1972) 79-89.
11. W. ZHANG; S. Xue; X. Hongyong, Chin. J. Process Eng. 4 (1) (2004) 509-514 .
12. M. A. Ismail; N. K. Memon; M. S. Mansour; D. H. Anjum; S. H. Chung, Proc. Combust. Inst. (2014).
13. H. Xie; G. Gao; Z. Tian; N. Bing; L. Wang, Particuology 7 (3) (2009) 204-210.
14. Y. Sung; V. Raman; R. O. Fox, Chem. Eng. Sci. 66 (19) (2011) 4370-4381.
15. Y. Gil; H. Jung; S. Chung, Combust. Flame 113 (3) (1998) 348-357.
16. D. Kim; Y. Gil; T. Chung; S. Chung, Combust. Sci. Technol. 181 (11) (2009) 1397-1412.
17. H. Zhao; X. F. Liu; S. D. Tse, J. Aerosol Sci. 40 (11) (2009) 919-937.
18. A. L. Patterson, Physical Review 56 (10) (1939) 978-982.
19. X. Y. Kong; Y. Ding; R. Yang; Z. L. Wang, Science 303 (5662) (2004) 1348-1351.
20. R. L. Penn; J. F. Banfield, Am. Mineral 83 (9-10) (1998) 1077-1082.